ISAC: Redefining the Vascular Segmentation Paradigm through Mask Completion for Cross-Domain Generalization

Tianyu Zhao[1], Zihang Huang[1], Xixi Jiang[2], Liang Zhang[1], Xiaohuan Ding[1], Xin Yang[1]✉

[1] School of Electronic Information and Communications, Huazhong University of Science and Technology
[2] Department of Electronic and Computer Engineering, The Hong Kong University of Science and Technology
xinyang2014@hust.edu.cn

Abstract. Accurate vessel segmentation is critical for diagnosis. However, the annotation of vascular images cost a lot, and due to their diverse modalities and complex foreground structures, it is hard for learning-based methods to reduce annotation cost by training models of high domain generalization (DG) on partial modalities. To address this, we propose the Image-Sparse Annotation Completion (ISAC) segmentation model, which reformulates vascular segmentation as a mask completion task based on sparse-annotated supports. ISAC treats the segmentation task as incomplete mask reconstruction guided by image features and structural properties of the foreground in the sparse mask. Unlike pixel-wise classification, ISAC detects vessels according to the mask context supported regions, in which way the anatomical continuity of vascular foreground is improved. Additionally, to further avoid the reliance on high-cost manually annotated supports, we propose the Uncertainty-guided Patch Selection (UPS) module to extract high-quality supports from coarse pseudo labels, which enables ISAC to perform segmentation in zero-shot scenarios. Experiments on 7 vascular datasets across 3 modalities demonstrate that ISAC outperforms state-of-the-art methods in DG ability. The code is publicly available at https://github.com/Architect15806/ISAC.

Keywords: Vascular Segmentation · Mask Completion · Domain Generalization.

1 Introduction

Accurate vessel segmentation is important in the diagnosis [21], such as detecting diabetic retinopathy in fundus images [2] or identifying coronary artery stenosis in X-ray coronary angiography images [20]. Learning-based models, as data-driven approaches, face challenges in training with diverse data due to various modalities and the high cost of manual annotation [8]. Thus, when confronted

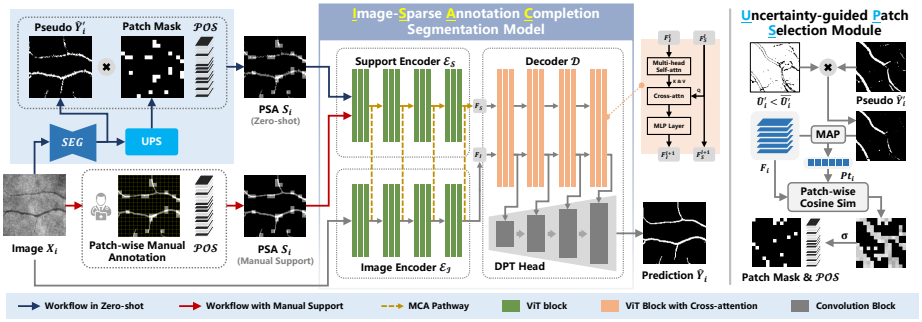

Fig. 1: Illustration of the proposed methods. (Left) The architecture of the proposed ISAC. (Right) The workflow of UPS. Patches in PSA with light gray background are visible to $\mathcal{E}_S$, while others are not. Patch Mask visualizes the POS sequence in an image-like format.

with domain shift due to the mismatch between test (target domain) and training (source domain) data, not only is the performance of existing segmentation methods prone to degradation, but even foundation models (e.g. MedSAM [32]) exhibit low accuracy (as shown in Table 2). Most existing methods formulate the segmentation task as pixel-wise classification [18], which is fundamentally **image-semantic correspondence (ISC)**. In vascular segmentation, specifically, these methods tend to focus on style-dependent high-frequency features rather than foreground structures [23]. This bias, combined with a lack of diversity in training data, results in limited domain generalization (DG) ability. To address this, [25] inversely fits ISC via extra reconstruction tasks, enabling the model to keep more domain-invariant foreground features.

[19,27,28] focus on filtering out style-related features through data augmentation. However, these methods still remain based on ISC. Other works based on few-shot learning (FSL) [5,4] obtain DG ability via prototype similarity within target domain. However, these methods are consequently limited by the uniformity of features across images. In addition, vascular foregrounds reflect **anatomical continuity**, helping human experts in annotation by tracking vessels within the context of identified segments. However, FSL-based methods cannot ensure continuity in the way of humans, as they calculate similarity on separate images rather than using the context within the image itself. Alternatively, some works [29,26] ensure anatomical continuity by designing loss functions based on vascular skeletons, yet they do not integrate this prior into their network architecture.

To address these challenges, we propose **Image-Sparse Annotation Completion (ISAC)** segmentation model, leveraging CroCo [31], a cross-view completion pretrained model. CroCo reconstructs missing parts of an incomplete view using spatial relationships with a complete view of the same scene. ISAC thus reformulates segmentation as a mask completion task based on **image-mask correspondence (IMC)** between vascular images and sparse annotated mask **supports**. The designed IMC task aims to reconstruct incomplete masks

based on the correspondence between images and sparse masks, therefore reduces domain shift effects by leveraging the structural characteristics of the supported foreground to focus more on style-invariant vascular morphological features. Different from FSL, ISAC not only adapts to unseen domains by implicitly utilizing image-support similarity, but also simulates vascular tracking by referencing context of mask in the support, thereby learning the anatomical continuity of vessels across adjacent regions. In some scenarios, acquiring even sparse manually-annotated masks is challenging. Thus, we design the **Uncertainty-guided Patch Selection (UPS) module** to extract high-quality supports from pseudo labels generated by other segmentation models, which enables ISAC to perform zero-shot segmentation without any manual annotations.

The contributions of our research are as follows: (1) We propose the ISAC model with strong DG ability for vascular segmentation by reformulating it as a mask completion task based on IMC, and improve the anatomical continuity of prediction by vascular tracking around the supported context of the mask. (2) We design the UPS module to extract high-quality supports from pseudo labels, enabling ISAC to perform zero-shot vascular segmentation. (3) To the best of our knowledge, we are the first to incorporate the cross-view completion model into segmentation tasks. We evaluate ISAC on 7 vascular datasets spanning 3 domains, and the results show that ISAC outperforms state-of-the-art (SOTA) methods across all datasets, highlighting its superior DG performance.

2 Method

We conduct our experiments using datasets from different domains: the source domain dataset $D_s = \{(X_i^s, Y_i^s, S_i^s)\}_{i=1}^{N_s}$ and the target domain dataset $D_t = \{(X_i^t, Y_i^t, S_i^t)\}_{i=1}^{N_t}$. The model will be trained in a fully supervised manner on D_s and tested on D_t. In each case, $X_i, Y_i \in \mathbb{R}^{H\times W}$ represent the image and its pixel-level segmentation annotation, while $S_i \in \mathbb{R}^{H\times W}$ represents the sparse annotation support. As shown in Fig 1, S_i is a patch-wise incomplete annotation instead of a pixel-wise one. Specifically, the image is pre-divided into patches ($\mathbb{R}^{d^2}$), each representing a local sub-region, and only a few are annotated while the rest remain unannotated. The positions of annotated patches are denoted as a sequence $\mathcal{POS} \in \{0,1\}^N$, where $\mathcal{POS} = 1$ marks the positions of annotated. We refer to such S_i as **Patch-wise Sparse Annotation Support (PSA)**.

The architecture of ISAC is shown in Fig 1. ISAC consists of a **dual-branch encoder** and a **support-guided decoder** (see Section 2.1). In the dual-branch encoder, the image branch $\mathcal{E}_I$ and the support branch $\mathcal{E}_S$ are respectively used to encode X_i and S_i as deep features F_I and F_S. Subsequently, under the constraint of $\mathcal{POS}$, the support-guided decoder $\mathcal{D}$ predicts the segmentation mask $\hat{Y}$ by fusing F_I and F_S. Moreover, to enable ISAC for zero-shot segmentation task without manually annotated S_i, we designed the **Uncertainty-guided Patch Selection Module (UPS)** to extract high-quality PSA $\hat{S}_i'$ from pseudo labels $\hat{Y}_i'$, which can be provided by other segmentation models (see Section 2.2). The loss function is described in Section 2.3.

2.1 Image-Sparse Annotation Completion Segmentation Model

Dual-Branch Encoder. $\mathcal{E}_I$ and $\mathcal{E}_S$ are independent Vision Transformer (ViT) [6] encoders with identical structures, where X_i and S_i are flattened into embeddings ($\mathbb{R}^{N\times d^2}$).

To alleviate the issue of contextual sparsity in $\mathcal{E}_S$ caused by PSA, we transfer contextual features from $\mathcal{E}_I$ via a Masked Cross-attention (MCA) pathway every 3 ViT layers:

$$\begin{gathered} x_S^{l+1} = \mathcal{POS}\cdot \mathrm{Attn}_1(y_I^l,\ y_S^l,\ y_S^l) + (1-\mathcal{POS})\cdot \mathrm{Attn}_2(y_I^l,\ y_S^l,\ y_S^l) \\ \mathrm{Attn}(Q,\ K,\ V) = \mathrm{softmax}\left(QK^T\right)V \end{gathered} \tag{1}$$

where x_S^l denotes the input of the l-th layer of $\mathcal{E}_S$, while y_I^l and y_S^l represent the outputs of the l-th layer of $\mathcal{E}_I$ and $\mathcal{E}_S$, respectively. Independent parameters are employed in Attn_1 and Attn_2 to process annotated and unannotated patches separately.

Support-guided Decoder. $\mathcal{D}$ is a dense-prediction transformer [22] (DPT)-based decoder guided by F_S. In each ViT block, embeddings from F_I are fused with F_S via cross-attention following Multi-Head Self-Attention, providing guidance for foreground segmentation. To achieve finer-grained vessel segmentation and alleviate bottleneck effects, we employ a full-resolution convolutional upsample path head to generate the model predictions. Specifically, the DPT head progressively reconstructs embeddings from the ViT layers into multi-scale image-like features at resolutions of 1/8, 1/4, 1/2, and full resolution. These features are subsequently fused layer-by-layer via concatenation and deconvolution to generate the final predictions.

2.2 Uncertainty-guided Patch Selection Module

In data-scarce scenarios, obtaining PSA can be challenging. Therefore, we propose the UPS to generate high-quality PSA using pseudo-labels $\hat{Y}_i'$ from any other segmentation model SEG trained on D_s. With the assistance of UPS, ISAC can perform zero-shot segmentation on unseen domains. Experiments show that using $\hat{Y}_i'$ as PSA without discrimination harms ISAC's performance, as the pseudo-labels contain noise introduced by domain shift. Consequently, the proposed UPS aims to select patches with low noise from $\hat{Y}_i'$ as PSA. Inspired by [13,12], we perform patch selection with the combination of image uncertainty and prototype. Specifically, we set the variance of SEG's predictions on X_i across different noise levels as the uncertainty $\hat{U}_i'$.

$$\hat{U}_i' = \frac{1}{n}\sum_{j=0}^{n}[SEG(X_i + N(\mu_j, \sigma_j^2))]^2, \quad \hat{Y}_i' = SEG(X_i) \tag{2}$$

where $N(\mu_j, \sigma_j^2)$ is Gaussian noise. $\hat{U}_i'$ represents the pixel-level uncertainty of SEG of $\hat{Y}_i'$. Subsequently, via Mask Average Pooling (MAP), we extract the

prototype $Pt_i \in \mathbb{R}^C$ of low-uncertainty foreground where $\hat{U}_i'$ is below the mean. Then, we measure the average cosine similarity between Pt_i and the foreground features for each patch, and dynamically select the patch positions as $\mathcal{POS}$ for PSA by retaining only the top σ fraction.

$$Pt_i = \frac{1}{|\mathcal{F}_i|} \sum_{(j,k)\in\mathcal{F}_i} M_{ijk} \cdot F_{ijk}, \quad S_{ip} = \frac{1}{|\mathcal{F}_{ip}|} \sum_{(j,k)\in\mathcal{F}_{ip}} \frac{F_{ijk} \cdot Pt_i}{\|F_{ijk}\|\|Pt_i\|}$$
$$\mathcal{POS} = \left\{ \mathbf{1}_{\{S_{ip} \geq S_{(\lceil \sigma N \rceil)}\}} \right\}_{p=1}^{N} \tag{3}$$

where $\mathcal{F}_i$ and $\mathcal{F}_{ip}$ respectively denote the sets of all foreground pixels and the foreground pixels in the p-th patch in $\hat{Y}_i'$. $F_{ijk} \in \mathbb{R}^C$ represents the deep features extracted by SEG, where C is determined by the architecture of SEG.

2.3 Loss Function

Considering the class imbalance caused by the relatively small proportion of vascular foreground pixels, we adopt a combination of Dice Loss and BCE Loss as the basic loss function. Based on that, to encourage ISAC to learn the correspondence between X_i and S_i in $\mathcal{POS}$ regions, we assign an extra weight to the

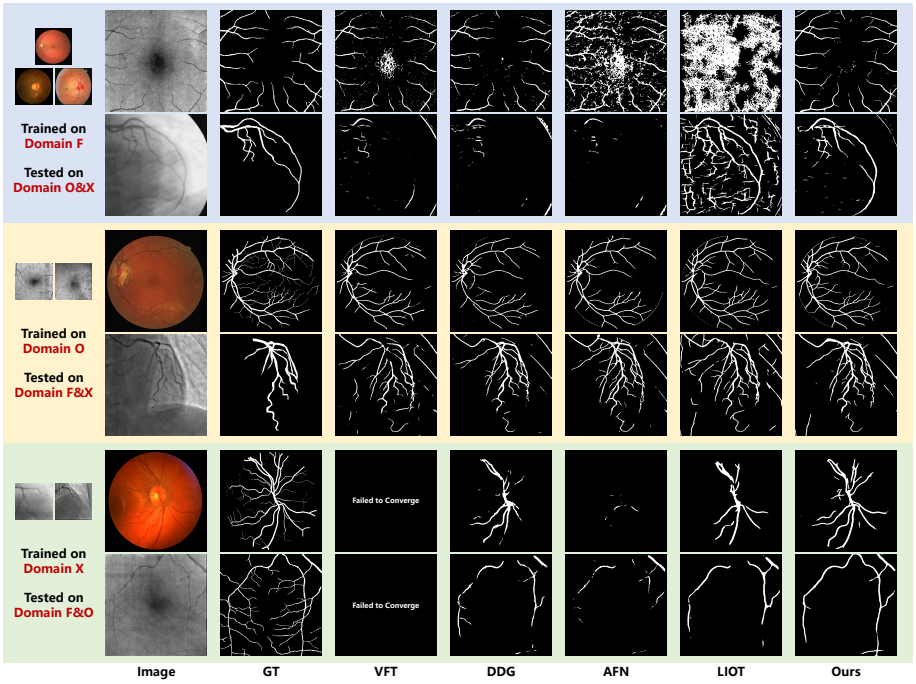

Fig. 2: Comparison of prediction visualization for DG scenarios between domains F, O, and X.

$\mathcal{POS}$ regions. Additionally, we introduce cldice [29] to emphasize the anatomical continuity around PSA, The loss function is formulated as follows:

$$\mathcal{L}_1(Y,\hat{Y}) = \lambda_1 \cdot \mathcal{L}_{wdice}(Y,\hat{Y},1+\mathcal{POS}) + \lambda_2 \cdot \mathcal{L}_{wBCE}(Y,\hat{Y},1+\mathcal{POS}) + \lambda_3 \cdot \mathcal{L}_{cldice}(Y,\hat{Y}) \tag{4}$$

where $\mathcal{L}_{wdice}$ and $\mathcal{L}_{wBCE}$ denote the weighted versions of the Dice and BCE loss functions respectively.

3 Experiments

3.1 Datasets and Experimental Details

Datasets. Our experiments utilize 7 public vascular datasets spanning 3 domains: **(1) Color Fundus (domain F) Datasets.** 3 datasets included: DRIVE (40 samples) [30], STARE (20 samples) [10], and CHASE_DB1 (28 samples) [7]. **(2) Optical Coherence Tomography Angiography (domain O) Datasets.** 2 datasets included: OCTA-500(6M) (300 samples) and OCTA-500(3M) (200 samples) [15]. **(3) X-ray Coronary Angiography (domain X) Datasets.** 2 datasets included: XCA (134 samples) [1] and XCAD (126 samples) [17]. All images are resized to 1024×1024 in experiments, and the input employs a sliding window strategy with a window size of 224×224, where adjacent windows overlap by 50%.

Experimental Details. ISAC is implemented in PyTorch on an NVIDIA 3090 GPU. The model is trained for 100 epochs with a batch size of 4 in each domain. The Adam optimizer is used with an initial learning rate of 2×10^{-5}, adjusted via CosineAnnealingLR. Loss function weights are set as $\lambda_1 = \lambda_2 = 0.5$ and $\lambda_3 = 1$. σ is set to 0.85. PSA is randomly selected from the ground truth (GT) during training and is provided either manually or by SEG during testing. 4 models

Table 1: Comparison with State-of-the-Art Methods in DG scenarios of domains F↔O and F↔X. A dash (-) indicates that the model fails to converge.

Model	DG	F1	CL	Prec	Acc	Rec	DG	F1	CL	Prec	Acc	Rec
VFT	F→O	43.45	39.46	52.02	91.70	41.54	F→X	41.44	39.40	49.57	94.49	41.82
	O→F	67.37	60.32	74.44	94.49	62.89	X→F	-	-	-	-	-
DDG	F→O	53.41	53.45	73.34	94.30	43.72	F→X	39.56	39.48	47.38	94.45	40.19
	O→F	65.82	61.46	**81.88**	94.65	56.41	X→F	51.00	42.02	**78.89**	93.19	38.61
AFN	F→O	44.39	42.81	39.42	85.13	**65.96**	F→X	41.39	39.79	47.90	94.26	48.33
	O→F	61.94	60.76	68.02	93.40	58.13	X→F	30.47	25.08	90.25	92.28	19.47
LIOT	F→O	58.31	56.16	59.97	93.65	57.97	F→X	37.94	34.41	29.70	89.94	**57.08**
	O→F	72.62	70.85	72.77	94.89	73.44	X→F	49.17	38.13	70.58	92.72	38.78
Ours	F→O	**60.49**	**62.03**	**75.03**	**94.81**	52.19	F→X	**52.86**	**53.96**	**53.90**	**94.91**	55.09
	O→F	**73.74**	**72.85**	75.63	**95.18**	**73.80**	X→F	**53.12**	**43.13**	78.56	**93.27**	**41.97**

Table 2: Comparison of prediction performance for different *SEG* and ISAC (†) based on corresponding *SEG* between domains F, O, and X.

	U-Net		**U-Net†**		**IterNet**		**IterNet†**		**SwinTR**		**SwinTR†**	
DG	**F1**	**CL**	**F1**	**CL**	**F1**	**CL**	**F1**	**CL**	**F1**	**CL**	**F1**	**CL**
F→O	23.30	24.47	59.11	59.23	52.21	52.69	60.49	62.03	32.92	30.64	60.15	60.74
F→X	27.25	24.82	52.84	52.17	38.46	38.94	51.94	53.98	25.31	21.02	52.38	52.49
O→F	67.07	60.47	73.95	72.48	63.80	56.84	73.74	72.85	67.03	65.63	72.99	72.12
O→X	44.15	42.63	46.52	46.62	28.26	32.45	34.68	39.43	32.35	34.66	36.17	39.15
X→F	47.96	40.57	54.15	44.12	49.67	41.10	53.12	43.13	42.67	32.24	50.22	39.86
X→O	42.19	44.17	50.03	52.38	29.37	27.48	43.59	40.22	42.24	42.01	49.82	49.98
	MedSAM		**MedSAM†**		**LIOT**		**LIOT†**				**Manual†**	
DG	**F1**	**CL**	**F1**	**CL**	**F1**	**CL**	**F1**	**CL**			**F1**	**CL**
F→O	60.02	57.89	60.61	61.61	58.31	56.16	61.26	62.81			64.27	68.48
F→X	52.67	48.18	53.38	53.78	37.45	33.62	52.90	53.90			69.51	71.36
O→F	-	-	-	-	72.62	70.85	73.72	73.12			75.31	78.88
O→X	40.18	46.82	41.60	44.39	33.31	38.92	37.43	42.60			75.96	79.72
X→F	-	-	-	-	49.17	38.13	52.46	40.65			64.56	71.52
X→O	52.17	50.11	56.61	57.55	39.83	36.42	46.13	41.99			64.14	75.86

with varying performance are used as *SEG* to demonstrate the robustness of UPS: U-Net [24], SwinTR [9], IterNet [14] and MedSAM [16]. 5 metrics are used in evaluation: Dice Coefficient (F1), Centerline Dice Coefficient (CL) [29], Precision (Prec), Accuracy (Acc), and Recall (Rec).

3.2 Experimental Results

Comparison with State-of-the-Art Methods. In our experiments, we compare ISAC with state-of-the-art (SOTA) methods that focus on DG in medical image segmentation, including: VFT [11], DDG [3], AFN [28] and LIOT [27]. We present 2 groups of DG results in Table 1: one between **domain F** and **domain O**, and the other between **domain O** and the **domain X**. For a fair comparison, IterNet is used as *SEG* in the experiments. ISAC outperforms all compared SOTA methods in terms of F1 and CL scores across the DG scenarios above. Specifically, for F↔O DG, ISAC achieves F1 scores of 60.49% and 73.74%, which are 2.18% and 1.12% higher than SOTA methods respectively. The CL scores are 62.03% and 72.85%, surpassing the SOTA methods by 5.87% and 2.00% respectively. For F↔X DG, ISAC achieves F1 scores of 52.86% and 53.12%, exceeding the SOTA methods by 11.42% and 2.12% respectively. The CL scores are 53.96% and 43.13%, which are 14.17% and 1.11% higher than the SOTA methods respectively. Visual segmentation results are shown in Fig 2.

3.3 Ablation study

Impact of Different *SEG*. In the zero-shot scenario, the performance of ISAC is related to the pseudo label provided by *SEG*. Therefore, we test the

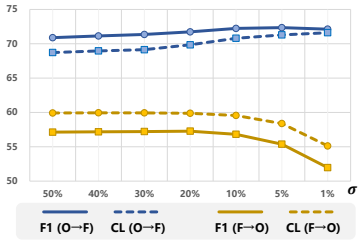

Fig. 3: Illustration of the Impact of σ on Segmentation Performance under F↔O DG.

Table 3: Illustration of the Impact of UPS and Cross-attention Pathway on Segmentation Performance under F↔O DG.

UPS	MCA	DG	F1	CL	Prec	Acc	Rec
×	×	F→O	56.73	59.34	74.84	94.48	47.05
		O→F	72.07	70.34	71.74	94.74	74.33
×	✓	F→O	56.73	59.38	74.91	94.49	47.03
		O→F	72.16	70.36	71.80	94.75	74.44
✓	×	F→O	57.20	59.84	75.06	94.54	47.53
		O→F	71.98	70.37	72.64	94.79	73.17
✓	✓	F→O	**60.49**	**62.03**	75.03	94.81	52.19
		O→F	**73.74**	**72.85**	75.63	95.18	73.80

performance of ISAC with different *SEG*, as shown in Table 2. (1) When using general baselines (U-Net, IterNet, or SwinTR) as *SEG*, ISAC consistently achieves better performance than the corresponding *SEG*. Even when the *SEG* performs poorly (e.g., U-Net for F→O), ISAC still provides relatively more accurate predictions. (2) When using the foundation model MedSAM with high DG ability as *SEG*, ISAC achieves higher performance compared to MedSAM in most DG scenarios. *(Since MedSAM is trained with domain F images, domain F is excluded from testing to ensure fairness.)* (3) When model designed for DG (LIOT) tasks acts as *SEG*, ISAC also achieves higher performance in all DG scenarios. Additionally, we tested ISAC with manually annotated support by randomly sampling from GT as PSA. As shown in the last column, the results show that ISAC with manually annotated PSA outperforms the zero-shot scenario.

Effectiveness of UPS and MCA Pathway. This experiment was conducted under the F↔O DG with IterNet as the *SEG*. First, the impact of σ in UPS is shown in Fig 3. The model achieves optimal performance when $\sigma \in [0.8, 0.9]$. Furthermore, with $\sigma = 0.85$, the effects of UPS and the MCA Pathway on model performance are presented in Table 3. The results demonstrate the necessity of both component. Since the workflow of ISAC relies on completing incomplete input segmentation masks, its performance is highly influenced by the quality of these PSA. Therefore, the introduction of the UPS module significantly enhances the model's overall segmentation performance. On this basis, the proposed MCA pathway further improves the fineness of segmentation masks by supplementing contextual information for sparse masks.

4 Conclusions

In this work, we propose Image-Sparse Annotation Completion (ISAC) Segmentation Model to tackle the challenges of DG and foreground discontinuity in vascular segmentation. ISAC reformulates segmentation as a mask completion

task using IMC instead of ISC, leveraging support to guide the model toward style-invariant vascular morphological features and thereby enhancing its DG ability in unseen domains. Notably, although ISAC has certain dependency on sparse annotations, the UPS module we designed can leverage the limited generalization ability of other segmentation networks to reduce this dependency. With the assistance of the UPS module, ISAC acquires the end-to-end segmentation capability in zero-shot scenarios. Experiments on 7 vascular datasets in 3 domains show that ISAC achieves SOTA performance in zero-shot DG, demonstrating its superiority over existing methods.

Acknowledgments. This work was supported in part by the National Natural Science Foundation of China under Grant 62472184, and in part by the Fundamental Research Funds for the Central Universities.

Disclosure of Interests. The authors have no competing interests to declare that are relevant to the content of this article.

References

1. Cervantes-Sanchez, F., Cruz-Aceves, I., Hernandez-Aguirre, A., Hernandez-Gonzalez, M.A., Solorio-Meza, S.E.: Automatic segmentation of coronary arteries in x-ray angiograms using multiscale analysis and artificial neural networks. Applied Sciences **9**(24), 5507 (2019)
2. Chen, C., Chuah, J.H., Ali, R., Wang, Y.: Retinal vessel segmentation using deep learning: a review. IEEE Access **9**, 111985–112004 (2021)
3. Cheng, Z., Liu, M., Yan, C., Wang, S.: Dynamic domain generalization for medical image segmentation. Neural Networks **184**, 107073 (2025)
4. Cheng, Z., Wang, S., Xin, T., Zhou, T., Zhang, H., Shao, L.: Few-shot medical image segmentation via generating multiple representative descriptors. IEEE Transactions on Medical Imaging (2024)
5. Ding, H., Sun, C., Tang, H., Cai, D., Yan, Y.: Few-shot medical image segmentation with cycle-resemblance attention. In: Proceedings of the IEEE/CVF Winter Conference on Applications of Computer Vision. pp. 2488–2497 (2023)
6. Dosovitskiy, A., Beyer, L., Kolesnikov, A., Weissenborn, D., Zhai, X., Unterthiner, T., Dehghani, M., Minderer, M., Heigold, G., Gelly, S., Uszkoreit, J., Houlsby, N.: An image is worth 16x16 words: Transformers for image recognition at scale. In: International Conference on Learning Representations (2021), https://openreview.net/forum?id=YicbFdNTTy
7. Fraz, M.M., Remagnino, P., Hoppe, A., Uyyanonvara, B., Rudnicka, A.R., Owen, C.G., Barman, S.A.: An ensemble classification-based approach applied to retinal blood vessel segmentation. IEEE Transactions on Biomedical Engineering **59**(9), 2538–2548 (2012)
8. Gao, S., Fu, Y., Liu, K., Xu, H., Wu, J.: Ka2er: Knowledge adaptive amalgamation of experts for medical images segmentation. arXiv preprint arXiv:2410.21085 (2024)
9. Hatamizadeh, A., Nath, V., Tang, Y., Yang, D., Roth, H.R., Xu, D.: Swin unetr: Swin transformers for semantic segmentation of brain tumors in mri images. In: International MICCAI brainlesion workshop. pp. 272–284. Springer (2021)

10. Hoover, A., Kouznetsova, V., Goldbaum, M.: Locating blood vessels in retinal images by piecewise threshold probing of a matched filter response. IEEE Transactions on Medical imaging **19**(3), 203–210 (2000)
11. Hu, D., Li, H., Liu, H., Oguz, I.: Domain generalization for retinal vessel segmentation via hessian-based vector field. Medical Image Analysis **95**, 103164 (2024)
12. Huang, Z., Wang, Z., Zhao, T., Ding, X., Yang, X.: Toward high-quality pseudo masks from noisy or weak annotations for robust medical image segmentation. Neural Networks **181**, 106850 (2025)
13. Huang, Z., Yang, Y., Zhao, T., Yang, X.: A noise robust framework via uncertainty guidance for medical image segmentation with noisy label. In: 2024 IEEE International Conference on Multimedia and Expo (ICME). pp. 1–6. IEEE (2024)
14. Li, L., Verma, M., Nakashima, Y., Nagahara, H., Kawasaki, R.: Iternet: Retinal image segmentation utilizing structural redundancy in vessel networks. In: Proceedings of the IEEE/CVF winter conference on applications of computer vision. pp. 3656–3665 (2020)
15. Li, M., Chen, Y., Yuan, S., Chen, Q.: Octa-500. IEEE Transactions on Medical Imaging **39**(9), 2806–2818 (2019). https://doi.org/10.1109/TMI.2020.2992244, https://doi.org/10.1109/TMI.2020.2992244
16. Ma, J., He, Y., Li, F., Han, L., You, C., Wang, B.: Segment anything in medical images. Nature Communications **15**(1), 654 (2024)
17. Ma, Y., Hua, Y., Deng, H., Song, T., Wang, H., Xue, Z., Cao, H., Ma, R., Guan, H.: Self-supervised vessel segmentation via adversarial learning. In: Proceedings of the IEEE/CVF International Conference on Computer Vision. pp. 7536–7545 (2021)
18. Nunes, I., Laranjeira, C., Oliveira, H., dos Santos, J.A.: A systematic review on open-set segmentation. Computers & Graphics **115**, 296–308 (2023)
19. Peng, L., Lin, L., Cheng, P., Huang, Z., Tang, X.: Unsupervised domain adaptation for cross-modality retinal vessel segmentation via disentangling representation style transfer and collaborative consistency learning. In: 2022 IEEE 19th International Symposium on Biomedical Imaging (ISBI). pp. 1–5. IEEE (2022)
20. Popov, M., Aimyshev, T., Ismailov, E., Bulegenov, A., Fazli, S.: A review of modern approaches for coronary angiography imaging analysis. arXiv preprint arXiv:2209.13997 (2022)
21. Qin, Q., Chen, Y.: A review of retinal vessel segmentation for fundus image analysis. Engineering Applications of Artificial Intelligence **128**, 107454 (2024)
22. Ranftl, R., Bochkovskiy, A., Koltun, V.: Vision transformers for dense prediction. In: Proceedings of the IEEE/CVF international conference on computer vision. pp. 12179–12188 (2021)
23. Ren, J., Zhang, X., Zhang, L.: Hifiseg: High-frequency information enhanced polyp segmentation with global-local vision transformer. arXiv preprint arXiv:2410.02528 (2024)
24. Ronneberger, O., Fischer, P., Brox, T.: U-net: Convolutional networks for biomedical image segmentation. In: Medical image computing and computer-assisted intervention–MICCAI 2015: 18th international conference, Munich, Germany, October 5-9, 2015, proceedings, part III 18. pp. 234–241. Springer (2015)
25. Shao, H.C., Chen, C.Y., Chang, M.H., Yu, C.H., Lin, C.W., Yang, J.W.: Retinatransnet: a gradient-guided few-shot retinal vessel segmentation net. IEEE Journal of Biomedical and Health Informatics (2023)
26. Shi, P., Hu, J., Yang, Y., Gao, Z., Liu, W., Ma, T.: Centerline boundary dice loss for vascular segmentation. In: International Conference on Medical Image Computing and Computer-Assisted Intervention. pp. 46–56. Springer (2024)

27. Shi, T., Boutry, N., Xu, Y., Géraud, T.: Local intensity order transformation for robust curvilinear object segmentation. IEEE Transactions on Image Processing **31**, 2557–2569 (2022)
28. Shi, T., Ding, X., Zhou, W., Pan, F., Yan, Z., Bai, X., Yang, X.: Affinity feature strengthening for accurate, complete and robust vessel segmentation. IEEE Journal of Biomedical and Health Informatics **27**(8), 4006–4017 (2023)
29. Shit, S., Paetzold, J.C., Sekuboyina, A., Ezhov, I., Unger, A., Zhylka, A., Pluim, J.P., Bauer, U., Menze, B.H.: cldice-a novel topology-preserving loss function for tubular structure segmentation. In: Proceedings of the IEEE/CVF conference on computer vision and pattern recognition. pp. 16560–16569 (2021)
30. Staal, J., Abràmoff, M.D., Niemeijer, M., Viergever, M.A., Van Ginneken, B.: Ridge-based vessel segmentation in color images of the retina. IEEE transactions on medical imaging **23**(4), 501–509 (2004)
31. Weinzaepfel, P., Leroy, V., Lucas, T., Brégier, R., Cabon, Y., Arora, V., Antsfeld, L., Chidlovskii, B., Csurka, G., Revaud, J.: Croco: Self-supervised pre-training for 3d vision tasks by cross-view completion. Advances in Neural Information Processing Systems **35**, 3502–3516 (2022)
32. Zhang, Y., Shen, Z., Jiao, R.: Segment anything model for medical image segmentation: Current applications and future directions. Computers in Biology and Medicine p. 108238 (2024)